fractal and fractional

MDPI

Article

Hybrid Fractal–Parametric Modeling and NSGA-II Optimization of Geometric Material-Volume Reduction in Generative Architectural Façades

Golib Berdiev [1,*], Shahzoda Anarova [2] and Navruz Khujakulov [3]

[1] Department of Information Technologies, University of Information Technologies and Management, Karshi 180100, Uzbekistan
[2] Department of Digital Technologies Convergence, Tashkent University of Information Technologies Named After Muhammad al-Khwarizmi, Tashkent 100084, Uzbekistan; anorova@tuit.uz
[3] Department of Software and Hardware Support of Computer Systems, Karshi State Technical University, Karshi 180100, Uzbekistan; xujaqulovnavruz1@gmail.com
* Correspondence: g.berdiyev@atmu.uz

Abstract

This study develops a hybrid fractal–parametric modeling (HFPM) workflow integrating recursive affine iterated-function systems, finite-scale box-counting, fixed-thickness prism extrusion, and NSGA-II to explore trade-offs between geometric material volume and geometric complexity in generative architectural façades. A common 729 × 729 raster and four box-counting scales (3, 9, 27, and 81) are applied to both investigated recursion depths (r = 3 and r = 4). Across five independent NSGA-II runs, the pooled final non-dominated reference set yielded geometric material-volume reductions of 34.58% and 44.57% within 1% and 2% deviations, respectively, from the baseline finite-scale fractal dimension (D_f). Mean hypervolume was 0.26182 ± 0.00113, evaluated in the original objective space against a common reference point (1.000000, 0.323566); mean inverted generational distance was 0.01732 ± 0.00244, evaluated using range-normalized distances to the empirical pooled reference front. Independent fixed-recursion optimization, simple branch-pruning controls, and density-seed, grid-origin, raster-resolution, and scale-window sensitivity tests further delimit these findings. Branch removal contributes substantially to the volume reductions, while the measured trade-offs and tolerance-feasible solutions depend on the chosen box-counting window. The results therefore establish a computational, protocol-dependent geometric trade-off for the investigated fixed-thickness prefractal prisms, not structural efficiency, equivalent façade functionality, fabrication feasibility, cost savings, or environmental benefits.

Keywords: fractal geometry; iterated function system; generative architecture; parametric façade; finite-scale box-counting; geometric material-volume reduction; NSGA-II; Pareto optimization

Check for updates

Academic Editors: Wei Cai, Xianglong Su and Wojciech Sumelka

Received: 25 September 2026
Revised: 20 October 2026
Accepted: 27 October 2026
Published: 5 November 2026

Copyright: © 2026 by the authors. Licensee MDPI, Basel, Switzerland. This article is an open access article distributed under the terms and conditions of the Creative Commons Attribution (CC BY) license.

1. Introduction

Computational architectural design has moved from the manual placement of predefined geometric elements toward rule-based and performance-driven systems in which form is generated, evaluated, and revised algorithmically. In this setting, a façade is not merely a static surface: it is a geometric system whose density, repetition, scale hierarchy, and thickness affect visual complexity, constructability, surface area, and the amount of material required. Generative design therefore creates an opportunity to treat façade development

as a search problem over a controllable geometric design space rather than as a sequence of isolated manual alternatives [1–3].

Fractal geometry is particularly relevant to this problem because it provides formal mechanisms for representing self-similarity and multi-scale organization. Mandelbrot established the modern conceptual basis of fractal geometry [4], while Hutchinson and Barnsley formalized self-similar sets and iterated function systems (IFS) as constructive mathematical mechanisms [5,6]. Falconer subsequently systematized the mathematical foundations of fractal dimensions and their measurement [7]. Within architecture, fractal concepts have been applied to design generation, formal analysis, and the quantitative characterization of visual complexity [8–20]. These studies show that architectural form can be investigated across several scales rather than through a single Euclidean descriptor.

For façade analysis, box-counting is one of the most frequently used estimators because it can be applied to finite drawings, images, or geometric projections. However, the result depends on image preparation, grid placement, selected scale intervals, and regression choices [11,12]. Recent engineering studies have further shown that scale parameters, counting origins, and scaling-window selection can materially affect estimated fractal dimensions [21,22]. Accordingly, the present study treats D_f as a finite-scale comparative descriptor computed under one fixed protocol rather than as an exact asymptotic Hausdorff dimension.

Parallel developments in parametric and generative design have made it possible to explore large families of alternatives and to couple geometric parameters with performance criteria [1–3,23–33]. Multi-objective evolutionary algorithms are particularly suitable when objectives conflict. In building and façade design, evolutionary optimization has been used to balance energy, daylight, comfort, esthetics, and other performance criteria [23–32]. The recent graph-enabled façade framework of Wang et al. [32], for example, integrates parametric generation with NSGA-II, while broader reviews show that façade engineering increasingly relies on multi-criteria and multi-objective computational methods [30].

Despite these advances, a methodological gap remains between three research streams: fractal generation, parametric control, and geometric material-volume-aware multi-objective optimization. Fractal studies in the built environment primarily quantify or interpret complexity [13–20], whereas performance-driven façade optimization often uses non-fractal geometric generators [29–32]. Conversely, fractal generative studies demonstrate recursive form-making but rarely formulate geometric material volume and finite-scale geometric complexity as simultaneous Pareto objectives. The present study addresses this integration gap through a Hybrid Fractal–Parametric Model (HFPM).

The research question is therefore: which fractal–parametric façade configurations can reduce modeled geometric material volume while keeping multi-scale geometric complexity close to a prescribed reference level? The contribution is methodological rather than structural: the study does not claim increased load-bearing capacity, equivalent architectural functionality, fabrication efficiency, lower embodied carbon, or reduced cost because these properties are not experimentally or structurally validated. Instead, it establishes and tests a reproducible computational pipeline linking recursive generation, parametric control, finite-scale geometric metrics, modeled prism volume, and repeated NSGA-II Pareto search. The methodological positioning of HFPM is summarized in Figure 1.

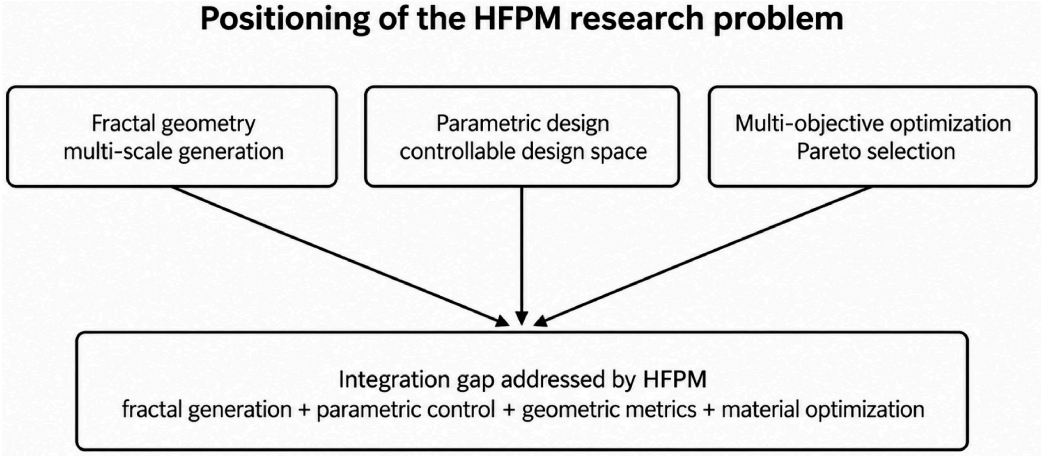


Figure 1. Positioning of the HFPM research problem at the intersection of fractal generation, parametric design, and multi-objective optimization.

The study makes four specific contributions: (**i**) a methodology-aligned affine IFS in which scale and rotation enter the recursive transformation matrix; (**ii**) a geometric evaluation layer with internal consistency checks separating finite-scale box-counting complexity, surface area, and material volume; (**iii**) a controlled design-space experiment that quantifies parameter effects before optimization; and (**iv**) an NSGA-II optimization that produces explicit material–complexity Pareto trade-offs and reproducible computational outputs.

2. Related Work

2.1. Fractal Geometry and Architectural Complexity

Architectural applications of fractal theory range from design criticism and visual analysis to direct algorithmic generation. Bovill [8] introduced fractal concepts as a design and analytical framework, while Ostwald and Vaughan developed a rigorous architectural box-counting methodology and emphasized the need to control scale and grid effects [9–11]. Vaughan and Ostwald distinguish between fractal inspiration, analytical interpretation, and algorithmic generation in architecture [10].

Recent work in Fractal and Fractional has reinforced the relevance of fractal analysis to the built environment. Lorenz and Kulcke [15] compared methods for evaluating self-similarity and architectural complexity; Kulcke and Lorenz [16] extended box-counting to observer-centered spherical panoramas; Ma et al. [17] developed a fractal-dimension-based visual complexity measure; Tara et al. [18] used voxelized 3D urban models; Ali and Mustafa [19] quantified façade complexity in office buildings; and Zhang et al. [20] compared 2D and 3D fractal characteristics of urban morphology. Katona's façade studies [13,14] further demonstrate the value of fractal measures for analyzing architectural composition. These studies support the use of fractal metrics in architectural analysis while also highlighting their dependence on representation and measurement protocol.

The present work differs by using the box-counting estimate not only for post hoc analysis but also as one objective in a generative optimization loop. Because the investigated objects are finite-depth prefactals represented on a raster grid, the notation D_f in this paper denotes a finite-scale box-counting estimate obtained over a declared set of box scales. It is used consistently as a comparative geometric complexity metric.

2.2. IFS, L-Systems, and R-Function-Based Geometric Construction

IFS represents a fractal object through repeated affine maps and is a natural mechanism for controlled recursive geometry [5,6]. L-systems provide a complementary grammar-based description of branching and rule-governed growth [34]. R-functions provide an

analytical framework for composing complex implicit geometric domains [35]. These three families of methods offer different but compatible ways of encoding recursive or composite geometry.

Within the authors' prior research context, R-function methods have been used to construct equations for national design patterns and fractal objects [36,37], while R-functions and L-systems have been integrated for geometric modeling of fractal-structured objects [38]. Related architectural studies by Rian and co-authors show how self-similar and random fractals can inform computational architectural structures [39,40] and how IFS can support generative structural truss design [41,42]. Anarova, Sadullaeva, and Berdiyev also investigated composition-based fractal analysis of building dimensions [43]. Unlike these earlier R-function/L-system studies and IFS-based truss-generation approaches, HFPM couples recursively composed affine IFS geometry with explicit scale, rotation, density and thickness controls, a declared finite-scale box-counting protocol, geometric material-volume evaluation, and multi-objective NSGA-II search within one reproducible workflow. This distinction motivates the present separation of geometry generation, measurement, and optimization.

2.3. Parametric Generative Design and Façade Optimization

Performance-driven generative design seeks to connect geometry generation with explicit evaluation criteria. Early integrated approaches demonstrated how generative geometry and performance models can operate within one design environment [1,2]. Turrin et al. [3] showed the benefits of combining parametric modeling with genetic algorithms for performance-oriented architectural exploration. In building optimization more broadly, genetic and multi-objective methods have been applied to green-building design [23], façade parameters [24], thermal and energy performance [25], and simulation-based building design [26–28].

Façade design is intrinsically multi-criteria. Yi [29] combined quantitative daylight performance with an esthetic-preference measure in multi-objective façade optimization, while Bianchi et al. [30] reviewed the state of the art in multi-criteria façade engineering and identified multi-objective optimization as a major direction. Zhang et al. [31] coupled parametric algorithms with generative residential design, and Wang et al. [32] combined graph-enabled façade generation with NSGA-II. Recent generative studies have also targeted material and structural efficiency in concrete and spatial-grid systems [33,44], while L-system-based parametric optimization has been applied to branching structural forms [45].

The optimization literature establishes NSGA-II as a mature method for bi-objective problems in which convergence and diversity must be maintained simultaneously [46–48]. Open-source multi-objective optimization frameworks have also supported reproducible experimentation and benchmarking [49]. However, the present research differs from conventional building-performance optimization because the decision space is generated by recursive fractal geometry and the second objective explicitly preserves a finite-scale fractal-complexity signature.

Table 1 summarizes the methodological gap addressed by HFPM.

Table 1. Comparative analysis of fractal, parametric, generative, and material-oriented approaches relevant to HFPM.

Approach	Fractal Generation	Parametric Control	Multi-Objective Optimization	Material-Volume Objective	Main Limitation
Classical fractal modeling	Yes	Partial	No	No	Primarily form/complexity

Table 1. *Cont*.

Approach	Fractal Generation	Parametric Control	Multi-Objective Optimization	Material-Volume Objective	Main Limitation
IFS/L-system generation	Yes	Yes	Usually separate	No	Optimization not intrinsic
Parametric generative design	Partial	Yes	Yes	Partial	Fractal generator not central
Façade multi-objective optimization	Partial	Yes	Yes	Task-dependent	Complexity usually non-fractal
Material-oriented generative design	Partial	Yes	Yes	Yes	Fractal complexity rarely explicit
Proposed HFPM	Yes	Yes	Yes	Yes	Requires geometric consistency checks and later structural/experimental validation

3. Materials and Methods

3.1. HFPM Overview and Parameter Space

The HFPM couples recursive affine generation, deterministic density control, 3D extrusion, geometric measurement, and NSGA-II optimization. The controlled design vector is

$$P = (r, s, \theta, d, t) \quad (1)$$

where r is recursion depth, s is the relative child scale, θ is the local rotation magnitude, d is the retained terminal-branch density, and t is façade thickness. The experimental façade envelope is a 6 m × 6 m square. To isolate the effects of recursive geometry from trivial thickness reduction, t was fixed at 0.08 m during the controlled experiments and optimization. The complete computational workflow is summarized in Figure 2.

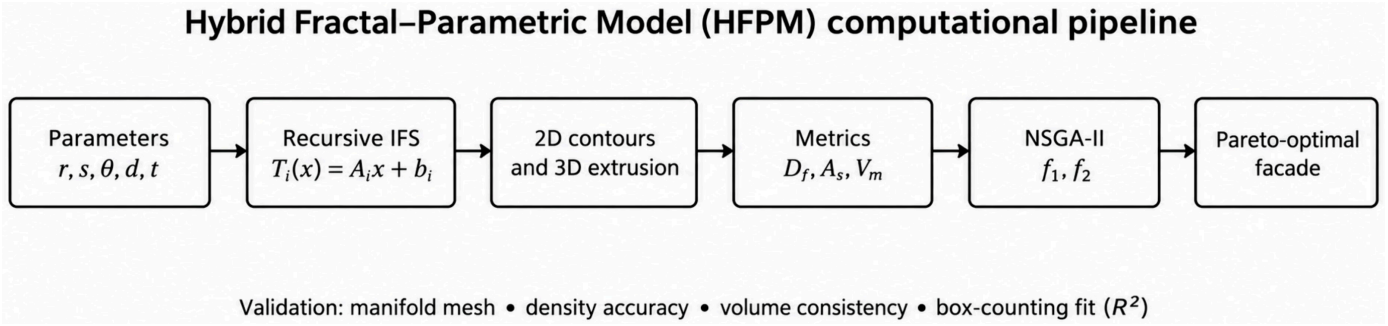


Figure 2. HFPM computational pipeline for recursive generation, global overlap checking, common-protocol finite-scale box-counting, geometric measurement, repeated NSGA-II optimization, and robustness analysis.

3.2. Methodology-Aligned Recursive IFS

The generative core uses eight affine child maps corresponding to the eight occupied positions of a 3 × 3 Sierpiński-carpet template. For child i, the recursive transformation is

$$T_i(x) = A_i x + b_i, i = 1, \ldots, 8 \quad (2)$$

$$A_i = \frac{s}{3} R(\theta_i) \quad (3)$$

$$R(\theta_i) = \begin{bmatrix} \cos\theta_i & -\sin\theta_i \\ \sin\theta_i & \cos\theta_i \end{bmatrix} \quad (4)$$

where $R(\theta_i)$ is a planar rotation matrix and θ_i alternates between $+\theta$ and $-\theta$ across child branches. Affine transforms are recursively composed, so scale and rotation propagate through the hierarchy rather than being applied only to terminal tiles. The canonical translation vector b_i locates each child in one of the eight non-central 3 × 3 positions. The contraction ratio is $q = s/3$.

To reduce local overlap risk, a conservative non-overlap constraint is imposed before recursive generation:

$$s(|cos\ \theta| + |sin\ \theta|) \leq 1 \tag{5}$$

The terminal set contains 8^r branches before density reduction. A deterministic ranking with fixed reference seed 42 retains exactly round$(d \times 8^r)$ terminal branches, which makes the realized density closely match the requested density. Because branch identity can alter finite-scale occupancy even when the retained count is unchanged, ten density-selection seeds are additionally evaluated for representative Pareto solutions. Global positive-area polygon intersections are also checked explicitly after generation rather than being inferred from the local constraint alone.

3.3. From 2D Prefactal Geometry to a 3D Façade

Each retained terminal affine map transforms a unit square into a planar quadrilateral inside the 6 m × 6 m façade envelope. The resulting quadrilateral is extruded by thickness t to produce a closed prism. All prisms are assembled into one Blender mesh for efficient evaluation. Material volume is computed analytically as the sum of terminal-prism volumes and independently checked against Blender's mesh-volume calculation. An additional global terminal-polygon overlap test verifies that no positive-area intersections remain in accepted configurations. All computational experiments were executed with Python 3.11 in Blender 4.5 LTS using the native bpy and bmesh APIs; the complete implementation is provided as Supplementary File S1.

$$S(P) = Extrude(C(P), t) \tag{6}$$

3.4. Geometric Metrics and Finite-Scale Box-Counting

Three geometric quantities are tracked separately: finite-scale box-counting dimension D_f, surface area A_s, and modeled geometric material volume V_m. This separation avoids treating fractal complexity as a proxy for physical material quantity. For the projected façade geometry, box-counting is estimated from

$$D_f \approx slope(log\ k, log\ N(k)) \tag{7}$$

where k is the number of boxes per side and $N(k)$ is the number of occupied boxes. All $r = 3$ and $r = 4$ configurations are rasterized on the same fixed 729 × 729 grid and evaluated with the same primary scale window $k = \{3, 9, 27, 81\}$. Ordinary least-squares regression is performed for $y = ln\ N(k)$ against $x = ln\ k$; the estimated slope is reported as the finite-scale D_f. The logarithm base does not affect the fitted slope when used consistently. At least four common scales are therefore used for the primary comparison, and accepted configurations must satisfy $R^2 \geq 0.95$. To assess sensitivity to the finite scaling window, two additional windows, $\{3, 9, 27, 81, 243\}$ and $\{3, 9, 27, 81, 243, 729\}$, are also computed. D_f is interpreted strictly as a finite-scale comparative descriptor under a declared common protocol, not as an asymptotic Hausdorff dimension.

$$A_s = \sum A_k \tag{8}$$

$$V_m = Vol[S(P)] \tag{9}$$

3.5. Baseline and Objective Functions

The reference façade is defined by $r = 4$, $s = 0.92$, $\theta = 0°$, $d = 1.00$, and $t = 0.08$ m. This baseline was selected as a dense, unthinned, unrotated reference state within the investigated parameterization: $r = 4$ represents the higher recursion level considered, $d = 1$ preserves the complete terminal topology, $\theta = 0°$ removes rotation-induced rearrangement, and $s = 0.92$ provides a large but admissible scale under the non-overlap constraint. The baseline is therefore a comparison state rather than a claimed engineering optimum. Under the common primary box-counting protocol, its measured values remain $D_{target} = 1.907744$ and $V_{ref} = 0.922751$ m^3. The 6 m × 6 m solid slab of the same thickness has a volume of 2.88 m^3, but optimization is referenced to the fractal baseline rather than to the solid panel.

$$f_1(P) = \frac{V_m(P)}{V_{ref}} \tag{10}$$

$$f_2(P) = \frac{\left|D_f(P) - D_{target}\right|}{D_{target}} \tag{11}$$

Thus, f_1 measures geometric material-volume ratio relative to the baseline and f_2 penalizes departure from the baseline finite-scale complexity. Pareto dominance is used rather than a weighted scalar objective so that the geometric material-volume–complexity trade-off remains explicit.

3.6. Controlled Design-Space Experiment

Before evolutionary optimization, 300 non-baseline configurations were generated using constrained Latin-hypercube-style stratification of the admissible parameter space [50]. Recursion levels $r = 3$ and $r = 4$ were balanced (150 cases each). Independent stratified columns were generated for θ, d, and scale position; each stratum was sampled once and then shuffled. Because the admissible upper bound of s depends on θ through Equation (5), each stratified scale coordinate was mapped into the local interval $[0.55, \min(0.95, \mathrm{slim}(\theta) - 10^{-4})]$. This preserves stratification while respecting the geometric constraint. The experiment therefore provides balanced recursion coverage and approximately uniform marginal coverage of the continuous variables over the admissible domain without using optimization feedback. The controlled settings are summarized in Table 2, and the complete 300-configuration dataset is provided in Supplementary File S5.

Table 2. Controlled experimental settings.

Parameter	Symbol	Controlled Setting/Range	Role
Recursion depth	r	{3, 4}	Hierarchy depth and terminal count
Relative scale	s	0.55–0.95, subject to Equation (5)	IFS contraction and spacing
Rotation magnitude	θ	0–90°	Recursive branch orientation
Retained density	d	0.50–1.00	Fraction of terminal branches retained
Thickness	t	0.08 m (fixed)	3D extrusion thickness
Panel envelope	—	6 m × 6 m	Common comparison domain
Raster resolution	—	729 × 729	Common box-counting support
Primary box scales	k	{3, 9, 27, 81}	Identical D_f regression window for $r = 3$ and $r = 4$
Reference density seed	—	42	Deterministic branch ranking; sensitivity tested separately

3.7. NSGA-II Optimization

NSGA-II was applied to the same parameterization [46]. Each run used a population of 40, 15 generations, crossover probability 0.90, mutation probability 0.20, and BLX-$\alpha = 0.25$ [51]. Integer recursion depth was restricted to {3, 4}; continuous variables were repaired to their admissible ranges after crossover and mutation. To assess stochastic robustness, five independent optimization runs were performed with seeds 4201, 7301, 10,401, 13,501, and 16,601. Duplicate parameter vectors were cached within each run to avoid repeated Blender evaluations. Invalid candidates received a large objective penalty and could not enter the final Pareto front. Non-dominated sorting and crowding distance were recomputed each generation. Final-front quality was quantified using two-dimensional hypervolume and inverted generational distance (IGD) relative to the pooled non-dominated reference set from all five runs. An equal-budget analysis compared the first 300 non-baseline NSGA-II evaluations of each run with the 300 balanced non-adaptive configurations.

A configuration was accepted as internally consistent only when all of the following held: (i) the mesh was manifold and free of degenerate faces; (ii) density error was ≤ 0.01; (iii) the relative difference between analytical and Blender volume was $\leq 10^{-5}$; (iv) the common four-scale box-counting regression was available; (v) D_f regression R^2 was ≥ 0.95; and (vi) the global terminal-polygon test detected no positive-area overlaps. These are internal geometric and numerical consistency checks, not structural, fabrication, or experimental validation. The measurement protocol and acceptance criteria were fixed before the repeated optimization runs.

3.8. Sensitivity and Independent Control Experiments

To evaluate the stability and specificity of the geometric material–complexity trade-off, three additional independent fixed-recursion NSGA-II searches were carried out with r fixed at 4 and optimization seeds 20,261, 20,262, and 20,263. These searches were not obtained by filtering the original variable-recursion runs. A separate simple branch-pruning control tested 21 density levels under ten branch-selection seeds (210 configurations). Since this control does not optimize s or θ, it provides an interpretable geometric reduction baseline but not an algorithmically equivalent head-to-head benchmark.

Density-selection sensitivity was extended to 20 sampled configurations with ten independent density-selection seeds per configuration (200 evaluations). Grid-origin and raster-resolution sensitivity were examined for 21 configurations at two raster resolutions (729×729 and 972×972) and four grid-offset settings per resolution (168 evaluations). The outcome of interest was the observed spread in the finite-scale box-counting estimate; these tests do not establish equivalence of architectural functionality. The prespecified four-scale protocol remained the primary optimization objective, while alternative windows and raster choices served only as diagnostic sensitivity checks.

Pareto quality was summarized using two-dimensional hypervolume (HV) and inverted generational distance (IGD), with both objectives (f_1, f_2) minimized. For HV, the same reference point (1.000000, 0.323566) was used for all runs. This point was chosen from the pooled non-dominated results with a 5% margin and lower bounds of 1.0 for f_1 and 0.05 for f_2. HV measures the dominated area bounded by this reference point in the original, unnormalized objective space. For IGD, a pooled empirical non-dominated reference set was formed from the five evaluated runs. Distances between each pooled reference solution and the nearest solution of a particular run were calculated after scaling each objective by its range across that pooled reference set; IGD is the mean of those distances. Because the evaluated runs themselves contribute to the IGD reference set, IGD quantifies within-study front consistency, not convergence to an independently established or true Pareto

front. The HV reference point is likewise data-derived and should not be interpreted as an independently prespecified external performance threshold.

4. Results

4.1. Computational Consistency and Dataset Quality

Across the five independent NSGA-II runs, the optimizer evaluated on average 600.6 unique non-baseline configurations per run, of which 599.6 on average passed all predefined internal geometric and numerical consistency checks. The mean final Pareto-set size was 38.0. The common box-counting baseline was $D_f = 1.907744$, with $R^2 = 0.999621$, and the baseline modeled material volume remained $V_m = 0.922751$ m^3. No positive-area global terminal-polygon overlaps were detected in the balanced sample or in the five repeated optimization runs. These checks establish internal computational consistency only; they do not demonstrate structural or construction performance. Summary metrics are reported in Table 3. Complete evaluation data and pooled Pareto outputs are provided in Supplementary Files S2 and S3.

Table 3. Computational consistency summary across five independent NSGA-II runs.

Metric	Revised Value
Independent NSGA-II runs	5
Mean unique non-baseline evaluations per run	600.6
Mean internally consistent evaluations per run	599.6
Mean final Pareto-set size	38.0
Baseline D_f (common protocol)	1.907744
Baseline box-counting R^2	0.999621
Baseline modeled volume V_m	0.922751 m^3
Mean hypervolume	0.26182 ± 0.00113
Mean IGD to pooled reference	0.01732 ± 0.00244
Detected positive-area global overlaps	0

4.2. Pareto Trade-Off Between Material Volume and Multi-Scale Complexity

Pooling the non-dominated solutions from all five independent runs produced a reference Pareto set that preserved the main geometric material-volume–complexity trade-off. The best pooled solution within a 1% deviation from the baseline finite-scale D_f reduced modeled material volume by 34.58%. Within 2%, the best reduction was 44.57%; the corresponding reductions within 3% and 5% tolerances were 52.98% and 58.69%, respectively. These values are reported as geometric material-volume reductions in the modeled prisms and should not be interpreted as verified reductions in structural mass, cost, fabrication waste, or embodied carbon. The tolerance-specific pooled and repeated-run reductions are summarized in Table 4. Representative façade geometries are shown in Figure 3, the pooled objective space in Figure 4, and the corresponding D_f–V_m relationship in Figure 5.

Table 4. Pooled and repeated-run geometric material-volume reductions at increasing D_f tolerances.

D_f Tolerance	Pooled Best Reduction	Best Volume Ratio	Five-Run Mean Reduction	SD Across Runs
1%	34.58%	0.6542	31.55%	3.53%
2%	44.57%	0.5543	39.93%	2.85%
3%	52.98%	0.4702	46.24%	6.31%
5%	58.69%	0.4131	57.33%	1.19%

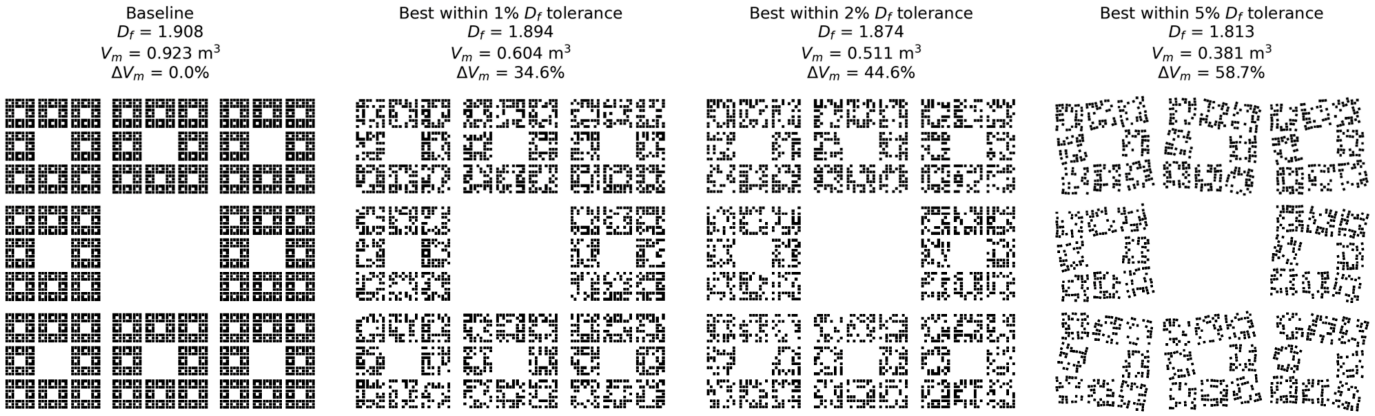


Figure 3. Baseline and representative pooled Pareto-optimal façade projections selected under 1%, 2%, and 5% allowable deviation from the baseline common-protocol finite-scale box-counting dimension.

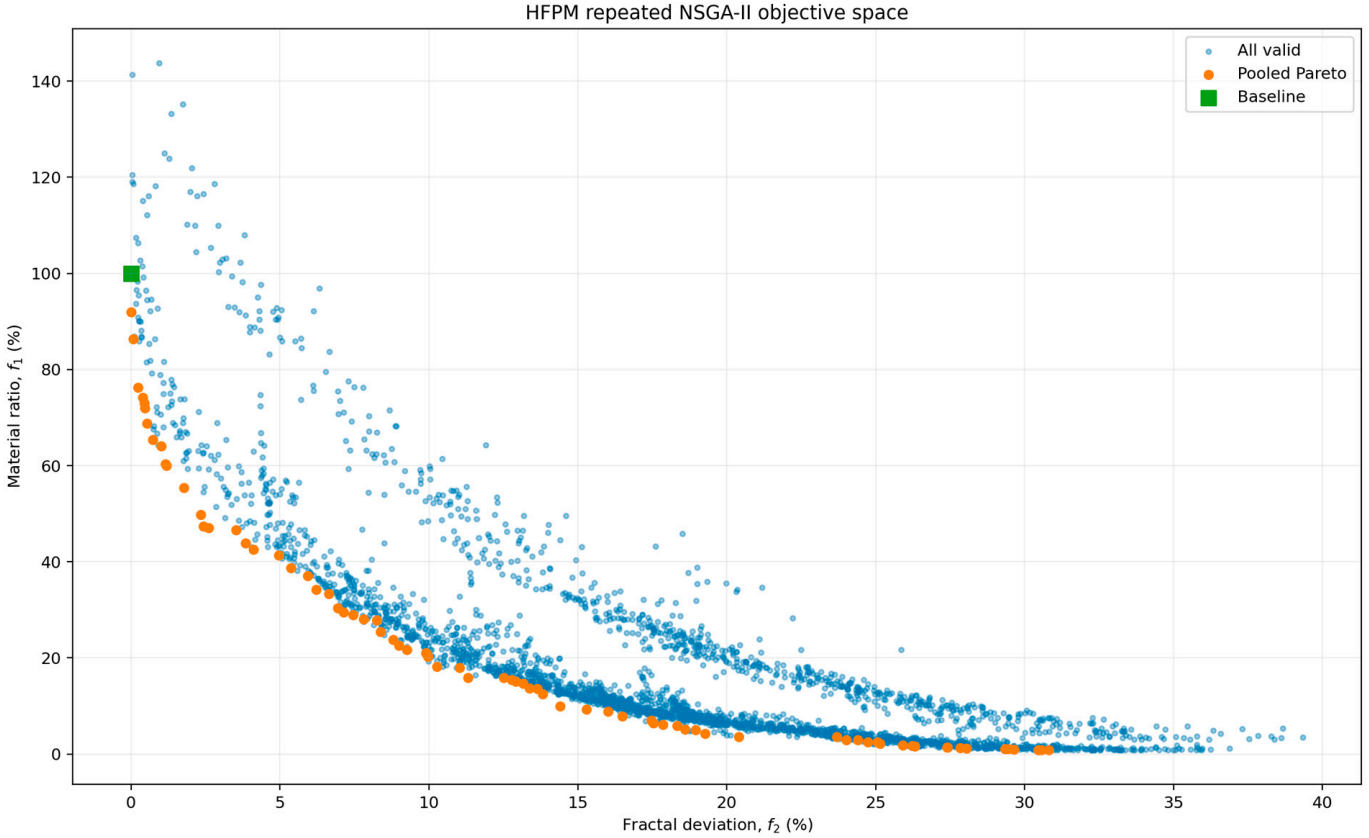


Figure 4. Repeated-run NSGA-II objective space. Blue points are internally consistent evaluations pooled across five independent runs, orange points form the pooled non-dominated reference set, and the green square is the baseline.

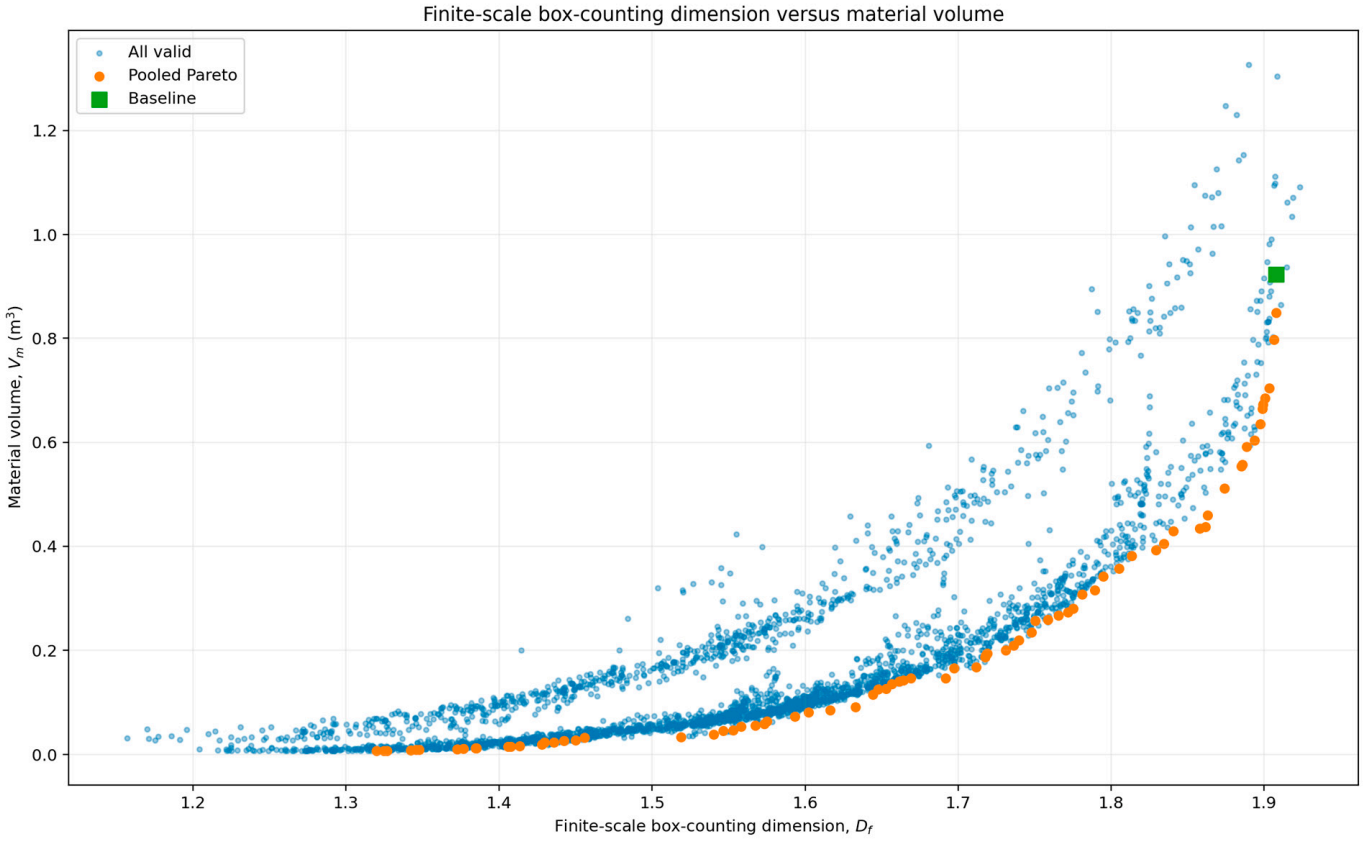


Figure 5. Relationship between common-protocol finite-scale box-counting dimension D_f and modeled geometric material volume V_m for the pooled NSGA-II evaluations.

4.3. Parameter Effects from the Balanced 300-Configuration Experiment

Because NSGA-II adaptively concentrates samples near favorable regions, parameter-effect analysis was performed on the balanced 300-configuration experiment. Under the common box-counting protocol, scale s remained the dominant monotonic control variable, with $\rho = 0.949$ for D_f and $\rho = 0.831$ for V_m. Retained density had smaller positive associations with D_f ($\rho = 0.206$) and V_m ($\rho = 0.247$). Rotation θ showed no statistically significant univariate monotonic association with either D_f ($\rho = 0.063$, $p = 0.277$) or V_m ($\rho = 0.067$, $p = 0.248$). Recursion level did not show a significant monotonic association with D_f ($\rho = 0.075$, $p = 0.195$) under the common scale window, although its association with V_m remained negative because additional recursive contraction can reduce terminal area in this parameter range. These Spearman results characterize monotonic marginal tendencies only and do not rule out nonlinear or interaction-dependent effects. The full correlation matrix is summarized in Table 5. Figure 6 illustrates the scale–volume relationship, Figure 7 shows retained density versus D_f, and Figure 8 shows rotation versus D_f.

Table 5. Spearman rank correlations from the balanced 300-configuration design-space experiment.

Parameter	ρ with D_f	p-Value	ρ with V_m	p-Value
Recursion level r	0.075	0.195	−0.500	3.35×10^{-20}
Scale s	0.949	1.98×10^{-151}	0.831	3.61×10^{-77}
Rotation θ	0.063	0.277	0.067	0.248
Retained density d	0.206	3.28×10^{-4}	0.247	1.68×10^{-5}

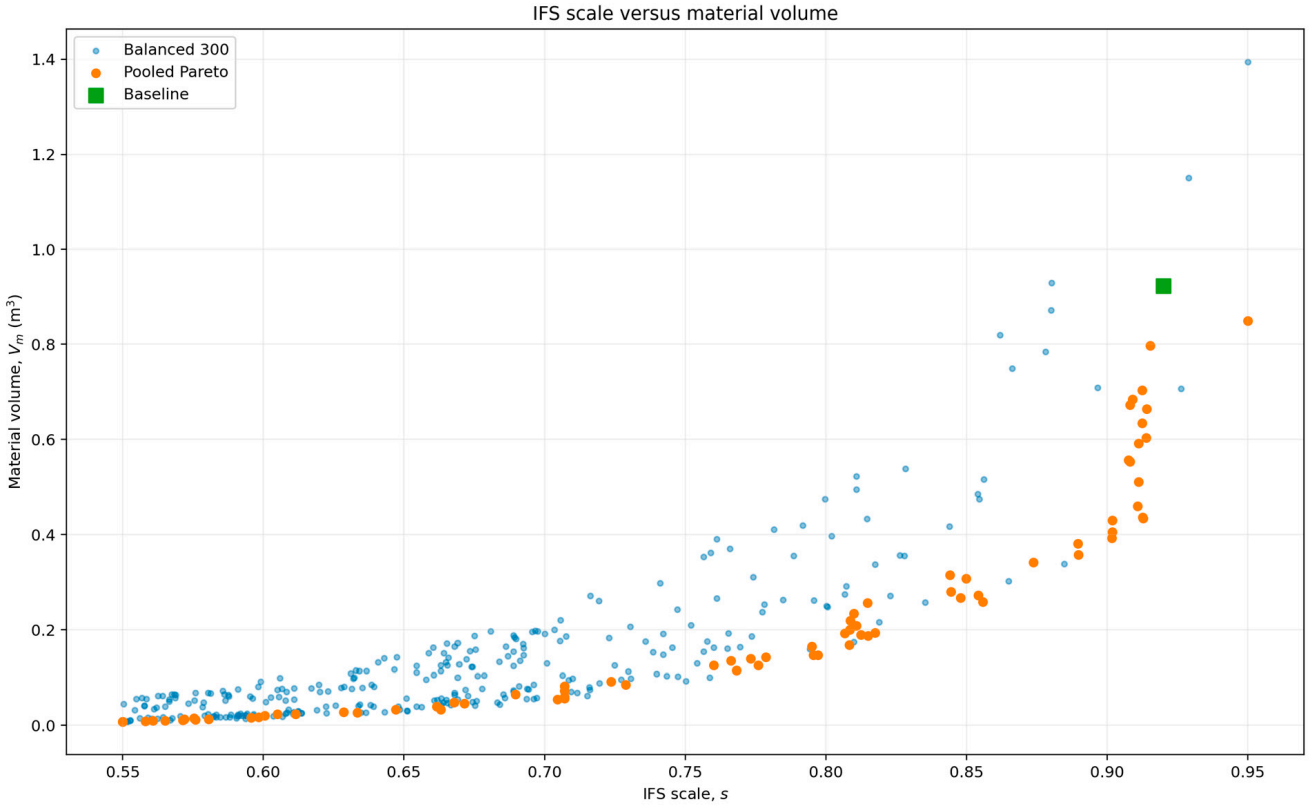


Figure 6. IFS scale s versus modeled geometric material volume V_m in the balanced 300-configuration experiment.

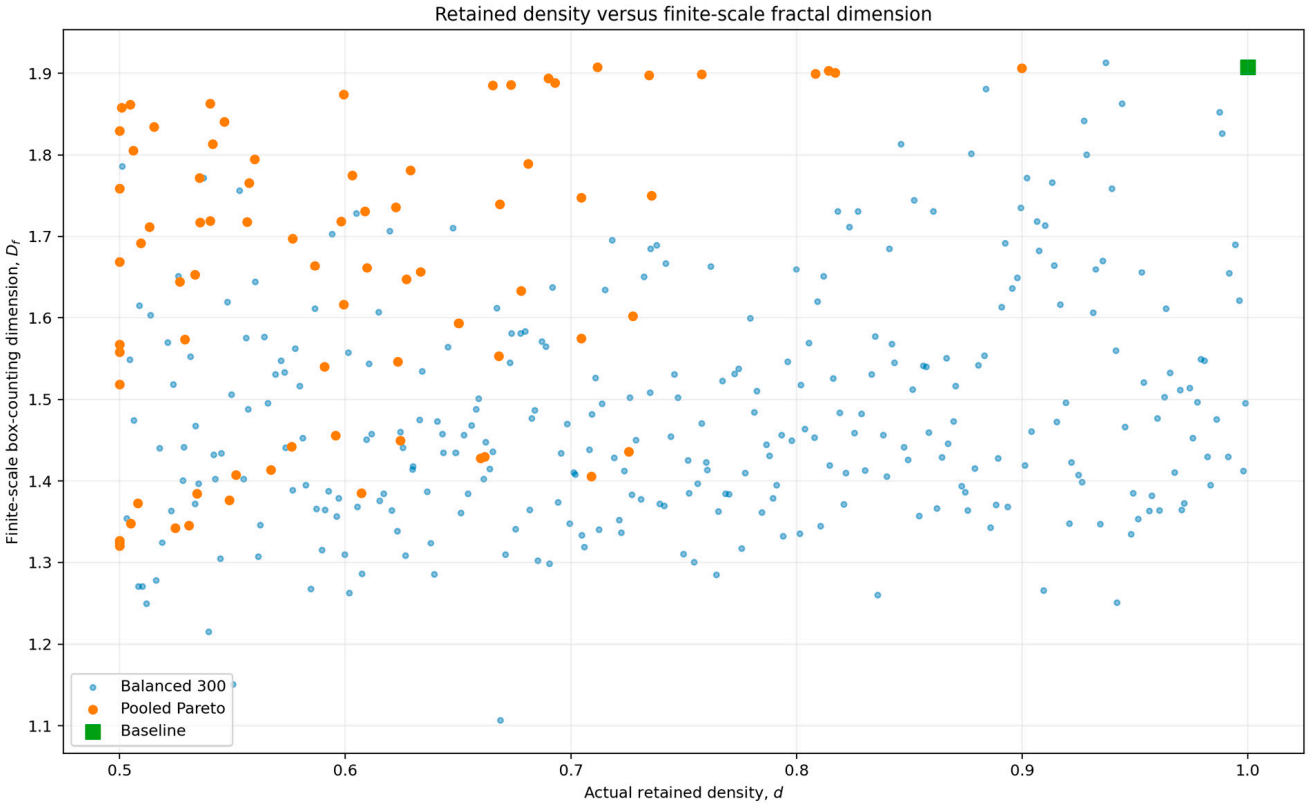


Figure 7. Retained branch density d versus common-protocol finite-scale box-counting dimension D_f in the balanced 300-configuration experiment.

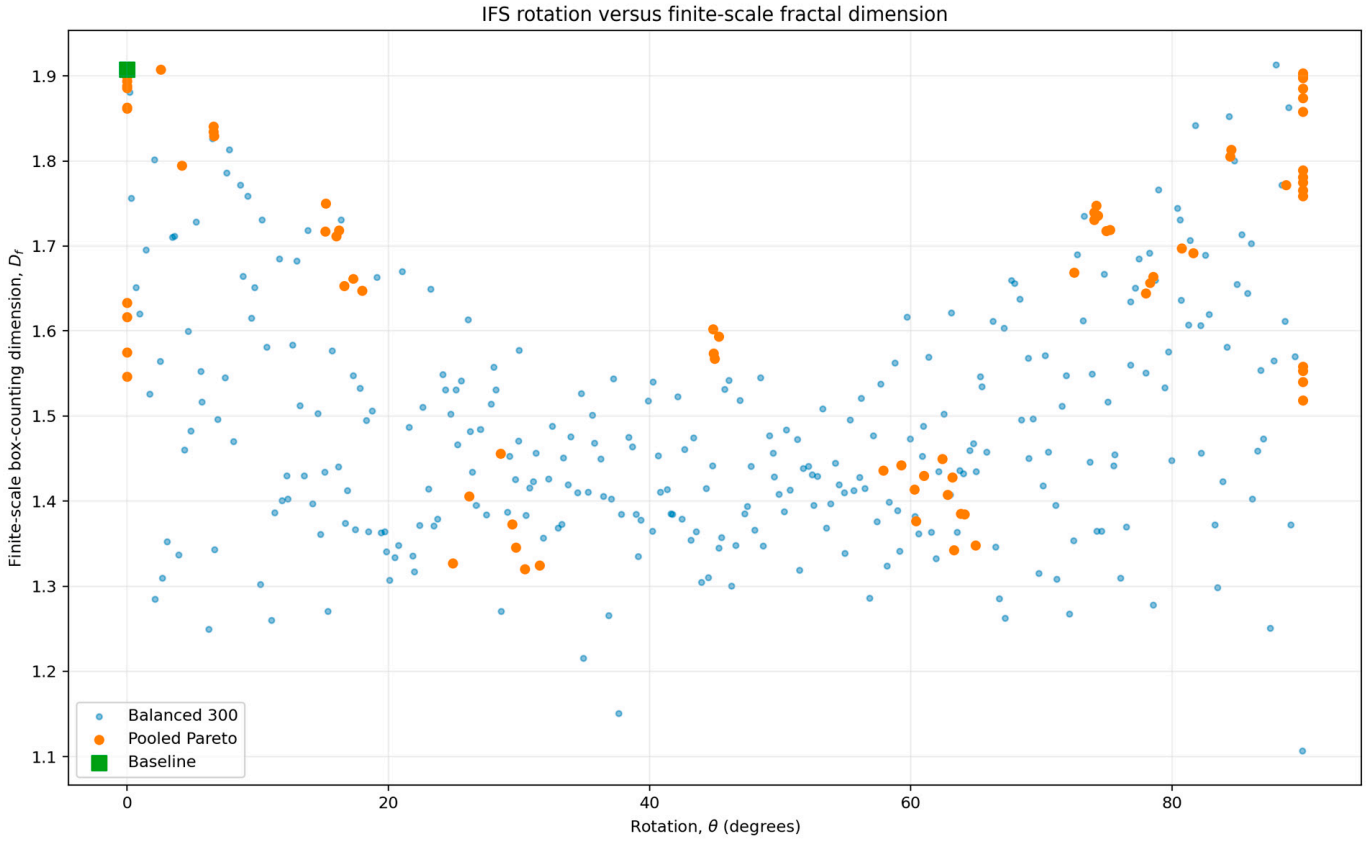


Figure 8. Rotation θ versus common-protocol finite-scale box-counting dimension D_f in the balanced experiment. The dispersed pattern is consistent with no significant univariate monotonic association; nonlinear and interaction effects are not excluded.

4.4. Repeated-Run NSGA-II Robustness and Equal-Budget Comparison

The five independent NSGA-II runs produced closely comparable Pareto-front quality. The mean two-dimensional hypervolume was 0.26182 ± 0.00113, and mean IGD to the pooled non-dominated reference set was 0.01732 ± 0.00244. Across runs, the best geometric material-volume reduction within a 1% D_f tolerance averaged 31.55% ± 3.53%; the corresponding averages were 39.93% ± 2.85% within 2%, 46.24% ± 6.31% within 3%, and 57.33% ± 1.19% within 5%. These repeated-run results show similar trade-offs across the five tested optimization seeds, without establishing robustness across all possible seeds or geometric settings. The mean convergence trajectories are shown in Figure 9.

For a budget-matched comparison, the first 300 non-baseline evaluations from each NSGA-II run were compared with the balanced 300-configuration sample. This places adaptive and non-adaptive search under an identical evaluation budget. The comparison confirms that adaptive Pareto search concentrates evaluations more effectively in favorable material-volume–complexity regions, particularly once moderate D_f deviations are permitted; the complete per-run 300-versus-300 results are supplied in Supplementary File S4. In the stored matched-budget results, mean NSGA-II best reductions across five runs were 23.49% at 1%, 24.82% at 2%, 29.99% at 3%, and 53.23% at 5% D_f tolerance, respectively. The single balanced sample yielded −51.06%, −24.67%, 23.16%, and 23.16% at these same thresholds. The negative balanced values at 1% and 2% indicate a tolerance-feasible candidate with volume above the baseline, not a positive material saving. The balanced sample is reused in each seed-wise comparison; therefore, the five comparisons are not five independent balanced-sampling replications, and no inferential superiority claim is made.

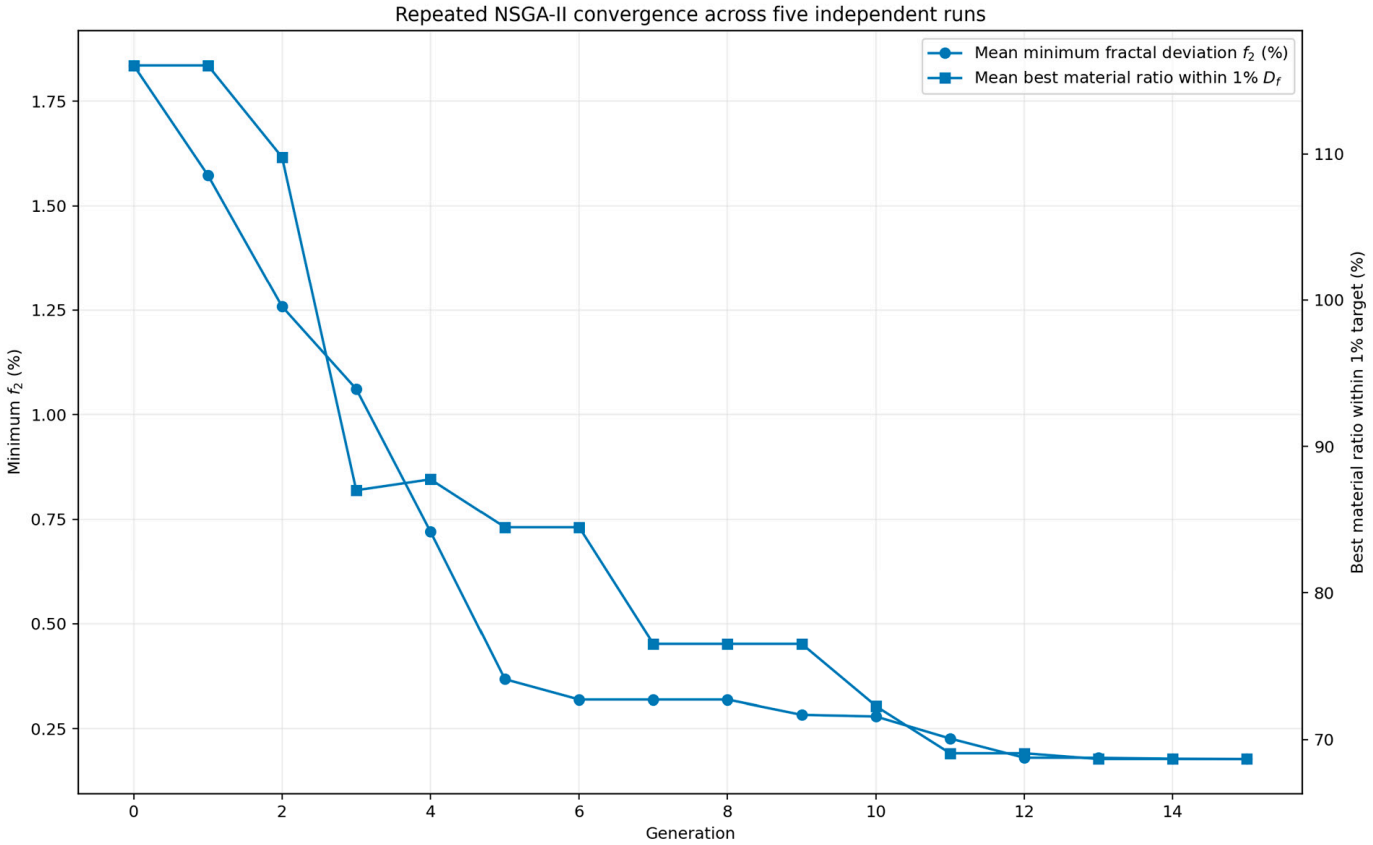


Figure 9. Mean NSGA-II convergence across five independent runs. The left axis shows the mean minimum fractal-deviation objective f_2 by generation; the right axis shows the mean best material ratio among solutions within 1% of the baseline D_f. Generation-level non-dominated front sizes and per-run convergence statistics are provided in Supplementary File S4.

4.5. Density-Seed Sensitivity and Fixed-Recursion Control

Density-selection sensitivity was assessed with ten deterministic seeds for five representative pooled Pareto solutions. Across these tests, the coefficient of variation in D_f ranged from 0.055% to 0.157%, while modeled material volume was effectively invariant (coefficient of variation below 3.4×10^{-8}) because the retained terminal count and affine scale determine prism volume at fixed parameters. Thus, branch identity has only a small effect on the finite-scale occupancy metric for the tested representative solutions.

A_s an initial within-dataset control, the five variable-recursion NSGA-II runs were filtered to $r = 4$; such filtering is descriptive and must not be presented as independent fixed-recursion optimization. To address this distinction, three additional NSGA-II searches explicitly constrained to $r = 4$ were performed, as reported in Section 4.6. Since density remains a design variable, the comparisons quantify modeled prism-volume and finite-scale complexity trade-offs rather than equivalent functional façade performance.

4.6. Independent Fixed-Recursion Optimization and Simple Branch-Pruning

The three genuinely independent fixed-$r = 4$ optimization runs returned 598, 596, and 609 valid candidate evaluations, with 37, 37, and 39 final non-dominated solutions, respectively. At 1% deviation from baseline D_f, no qualifying solution was found in run 20,261, whereas runs 20,262 and 20,263 attained 24.34% and 37.86% geometric volume reductions. At the 2% tolerance, the corresponding qualifying reductions were absent: 45.23% and 40.02%. This substantial run-to-run variation is reported explicitly; no zero reduction is imputed when no tolerance-feasible candidate is found. These experiments

show that reductions can be found without decreasing recursion depth, but do not support a claim of uniform near-baseline performance across optimization seeds.

The 210-configuration simple branch-pruning control attained best geometric volume reductions of 30.00%, 42.50%, 50.00%, and 50.00% within 1%, 2%, 3%, and 5% D_f tolerances, respectively. Pruning therefore explains part of the achievable material reduction independently of evolutionary parameter search. Because the pruning control explores a different parameter family and number of evaluations, these values are used to delimit the contribution rather than to assert superior algorithmic performance. The comparative results are summarized in Table 6.

Table 6. Independent fixed-recursion optimization and simple-pruning controls. The reported reductions are best observed geometric prism-volume reductions subject to the stated finite-scale D_f tolerance; "Not found" indicates that no eligible candidate was identified in that run.

Search/Control	Run/Seeds	Valid Eval.	1% D_f	2% D_f
Fixed $r = 4$ NSGA-II	20,261	598	Not found	Not found
Fixed $r = 4$ NSGA-II	20,262	596	24.34%	45.23%
Fixed $r = 4$ NSGA-II	20,263	609	37.86%	40.02%
Simple branch pruning	10 density seeds	210	30.00%	42.50%

4.7. Extended Density-Seed and Raster-Grid Sensitivity

Across 20 sampled designs evaluated with ten density-selection seeds each, the median coefficient of variation in D_f was 0.186% (range 0.032–0.416%). Modeled prism volume varied negligibly across seeds for fixed r, s, θ, d and thickness, consistent with a fixed retained-element count. These results extend the five representative-solution checks in Section 4.5, but they do not establish seed-invariance for arbitrary geometries.

Across 21 designs, the within-design four-offset range in D_f had a median of 0.0060 and a maximum of 0.0283 over the two tested raster resolutions. The median offset range was 0.0068 at 729 × 729 and 0.0051 at 972 × 972. Grid placement therefore introduces a nonzero finite-resolution uncertainty even under a fixed four-scale regression convention. The result should be understood as measurement sensitivity, not as a change in the physical prism geometry. Summary statistics are reported in Table 7.

Table 7. Extended density-seed and raster-origin sensitivity experiments.

Diagnostic	Sample Size	Observed Result
Density-seed variation	20 designs × 10 seeds	Median D_f CV 0.186%; range 0.032–0.416%
Grid origins, 729 × 729	21 designs × 4 offsets	Median D_f range 0.0068
Grid origins, 972 × 972	21 designs × 4 offsets	Median D_f range 0.0051
Both resolutions	168 evaluations	Maximum within-design offset range 0.0283

The scaling-window sensitivity was additionally quantified by rescoring the existing 2998 internally accepted optimization evaluation records. The four-, five-, and six-scale windows yielded different baseline D_f values and tolerance-feasibility counts. For a 1% D_f tolerance, the best observed geometric volume reductions were 35.72%, 9.87%, and 11.93%, respectively; the corresponding values within 2% were 44.57%, 27.10%, and 20.80%. Under the six-scale window, 112 of 2998 records failed the $R^2 \geq 0.95$ requirement (3.74%), compared with none under four or five scales. These are post hoc rescoring diagnostics of the existing configuration pool, not independently reoptimized Pareto fronts. Consequently, the quantitative savings are conditional on the predeclared primary four-scale estimator. The sensitivity outcomes and acceptance counts for each window are reported in Table 8;

unlike the main five-run Pareto summary in Table 4, these values are best observations from rescored existing evaluation records and do not represent newly optimized fronts. The 35.72% four-scale result refers to the best recorded configuration among all 2998 internally accepted evaluation records (config. 5,000,509), including candidates excluded from the final-generation Pareto archives; the 34.58% result in Table 4 refers strictly to the pooled final-run Pareto reference set (config. 5,000,435). These are different selection populations, not conflicting volume measurements.

Table 8. Post hoc scaling-window sensitivity for the existing evaluated configuration pool; best observed reductions are not the pooled Pareto-front outcomes of Table 4.

Metric	4 Scales	5 Scales	6 Scales
Baseline D_f	1.907744	1.856400	1.809520
Accepted records ($R^2 \geq 0.95$)	2998	2998	2886
Within 1%: best reduction	35.72%	9.87%	11.93%
Within 2%: best reduction	44.57%	27.10%	20.80%

5. Discussion

5.1. Interpretation of the Material–Complexity Trade-Off

The central finding is not that a single "optimal" façade exists, but that HFPM exposes a reproducible trade-off between finite-scale geometric complexity and modeled geometric material volume. The pooled repeated-run Pareto set contains solutions for designers who prioritize close preservation of the baseline multi-scale signature as well as solutions that accept larger geometric deviation in exchange for greater prism-volume reduction. This representation is more appropriate for early-stage computational exploration than a single weighted optimum because the relative value assigned to geometric complexity and material reduction is project-dependent.

The common-scale analysis shows that the principal trade-off remains under an identical box-counting protocol for both recursion depths. The pooled reference set produced a 34.58% geometric material-volume reduction within 1% of the baseline D_f and 44.57% within 2%. These results arise from a common measurement protocol and five independent optimization runs. They should be interpreted only as geometric reductions in the modeled façade prisms, not as verified savings in embodied carbon, cost, structural mass, fabrication waste, or installed façade material.

The separation of D_f, A_s, and V_m is methodologically significant. Earlier architectural fractal research primarily uses fractal dimension to measure or interpret visual and structural complexity [13–20]. HFPM adds a second, physically dimensioned quantity—material volume—without assuming that higher or lower D_f directly implies better material efficiency. The Pareto front shows that the relationship is not one-to-one; several geometries with similar D_f have substantially different V_m.

5.2. Relation to Generative and Façade Optimization Research

The results extend the performance-driven generative design paradigm established by Shea et al. [1], Turrin et al. [3], and later building-optimization studies [23–28] by making recursive fractal geometry itself part of the decision space. Compared with façade optimization studies that use daylight, energy, or aesthetic-preference objectives [29,32], HFPM uses a deliberately narrower objective pair to isolate the interaction between finite-scale geometry and modeled material volume. The method is therefore complementary rather than competitive: energy, daylight, structural, fabrication, and life-cycle criteria

would be required before any claim of engineering-equivalent façade performance could be made.

Recent generative structural research reports substantial material savings through topology or layout optimization [33,44]. Numerical reductions in a similar order can occur in HFPM, but their physical meaning is different. The spatial-grid study of Wang et al. [44], for example, incorporates finite-element structural evaluation, whereas HFPM does not. Consequently, this paper restricts its conclusion to geometric material-volume reduction under the stated extrusion, density, and non-overlap assumptions and does not claim structural efficiency or equivalent architectural functionality.

5.3. Why Scale Dominates and Rotation Does Not Show a Global Monotonic Effect

The balanced design-space experiment confirms that s is the strongest monotonic driver of both D_f and V_m. This is partly inherent to the recursive construction: scale changes the area of every terminal branch at every recursion level, so its effect is compounded geometrically. The strong correlation should therefore be interpreted as both an empirical sensitivity result and an expected structural consequence of the generator, rather than as an independent causal discovery.

In contrast, θ primarily redistributes orientation and local spacing. Under the conservative local constraint and explicit global-overlap check, rotation does not directly change the area of an individual transformed square. The non-significant Spearman coefficient therefore means only that no global univariate monotonic association was detected in the balanced sample; it does not exclude nonlinear responses or interactions of θ with s, r, and d. Future work should quantify these interactions using variance-based or surrogate-model sensitivity analysis.

5.4. Finite-Scale Fractal Measurement and Methodological Caution

The reported D_f values are finite-scale box-counting estimates calculated from rasterized prefactal projections. They should not be interpreted as exact Hausdorff dimensions of infinite IFS attractors. To ensure direct comparability across recursion depths, the same 729×729 raster and the same primary scales $\{3, 9, 27, 81\}$ are applied to every candidate and to the baseline. The reported slope is therefore directly comparable across $r = 3$ and $r = 4$ under one declared protocol.

Even with four common primary scales, the estimate remains finite-scale and potentially sensitive to scale-window and grid choices. Accordingly, the workflow also computes the larger windows $\{3, 9, 27, 81, 243\}$ and $\{3, 9, 27, 81, 243, 729\}$ as sensitivity analyses rather than selecting a favorable window post hoc. The common primary protocol is fixed for optimization, while alternative windows are used only to characterize measurement sensitivity. The grid-origin and alternative-resolution sensitivity tests are reported in Section 4.7; systematic extensions to additional resolutions, lacunarity and multifractal descriptors remain for future work.

The independent fixed-recursion searches and simple-pruning baseline qualify the methodological claim. Both approaches can obtain material-volume reductions near the target finite-scale D_f, but not with uniform feasibility over optimization runs. Simple pruning also obtains substantial reductions, demonstrating that reduced branch count is part of the mechanism rather than a unique benefit attributable to NSGA-II. The principal contribution remains the integrated geometric generator, transparent measurement protocol, and explicit exploration of Pareto trade-offs within the defined design space.

Sensitivity measurements also delimit what "preserved complexity" means: a small difference in one rasterized box-counting estimate does not imply invariant visual appearance, façade function, manufacturability or structural capacity. Alternative scale windows

and changes in grid origin can shift the measured descriptor and hence alter tolerance-feasibility judgments. The numerical findings should be read with their specific baseline, raster, regression window and tested optimization budget.

5.5. Limitations and Future Work

The current study has six main limitations. First, it is a geometric computational optimization study and does not include FEM, connection design, buckling, wind loading, fire performance, fabrication tolerances, or physical experiments. Second, façade thickness is fixed at 0.08 m to prevent trivial material reduction through thickness minimization; a future structural model should allow thickness to vary only under stress, deflection, and stability constraints. Third, the search is limited to two recursion depths and one eight-map affine topology. Fourth, the density operator removes terminal branches algorithmically and does not impose architectural program constraints such as windows, doors, views, drainage, or modular panelization. Fifth, modeled prism volume is only a geometric proxy; embodied carbon, cost, waste, connections, manufacturing, logistics, and service life are not represented. Sixth, finite-scale D_f remains dependent on the declared raster and scaling window despite the common-scale protocol and scaling-window sensitivity analyses. The primary four-scale regression is retained as an operational finite-scale descriptor, not evidence of an asymptotic fractal dimension; the alternative scaling windows change tolerance-feasibility and observed reductions appreciably (Table 8).

Future development should therefore integrate (i) finite-element structural analysis, (ii) daylight and thermal simulation, (iii) fabrication and minimum-feature constraints, (iv) embodied-carbon factors, and (v) additional fractal descriptors. Surrogate modeling could also reduce the computational cost of higher-dimensional multi-objective searches [26–28]. A particularly useful next step is a constrained three- or four-objective model balancing material volume, D_f, structural performance, and environmental performance while retaining the same reproducible geometric core.

6. Conclusions

This study developed and computationally evaluated an HFPM workflow for exploring finite-scale fractal-complexity versus geometric material-volume trade-offs in modeled architectural façade prisms. All $r = 3$ and $r = 4$ configurations used the same 729×729 raster and primary box-counting window $k = \{3, 9, 27, 81\}$. Across five independent NSGA-II runs, the pooled final non-dominated set yielded geometric material-volume reductions of 34.58% and 44.57% within 1% and 2% of the baseline D_f, respectively. Mean HV and IGD were 0.26182 ± 0.00113 and 0.01732 ± 0.00244 under their declared, different reference and normalization conventions; the IGD reference set is empirical and pooled from those runs. Independent fixed-recursion optimization and branch-pruning controls show that removing terminal branches explains an important portion of achievable volume reduction. Alternative scale windows and raster-grid sensitivity checks show that the numerical trade-offs depend on the finite-scale measurement protocol. These outcomes support an integrated computational method for examining geometric Pareto choices within the investigated design space, but do not demonstrate superior performance over all geometric baselines or equivalence of visual, architectural, structural, fabrication, economic, or environmental functionality.

Supplementary Materials: The following supporting information can be downloaded at: https://www.mdpi.com/article/10.3390/fractalfract10110771/s1, S1–S6 contain the HFPM implementation, repeated-run evaluation datasets, Pareto sets, robustness and convergence summaries, balanced design-space data, and figure-regeneration code. S7 contains independently generated fixed-recursion, simple branch-pruning, density-seed, and raster-origin control data. S8 contains alternative scale-window rescoring diagnostics. All materials are provided in "HFPM_Supplementary_Materials".

Author Contributions: Conceptualization, G.B. and S.A.; methodology, G.B., S.A. and N.K.; software, G.B. and N.K.; validation, G.B. and N.K.; formal analysis, G.B. and S.A.; investigation, G.B., S.A. and N.K.; resources, S.A. and N.K.; data curation, G.B. and N.K.; writing—original draft preparation, G.B.; writing—review and editing, G.B., S.A. and N.K.; visualization, G.B. and N.K.; supervision, S.A.; project administration, G.B. All authors have read and agreed to the published version of the manuscript.

Funding: This research received no external or institutional funding.

Institutional Review Board Statement: Not applicable. The study did not involve humans or animals.

Informed Consent Statement: Not applicable.

Data Availability Statement: The computational data supporting the principal optimization findings are included in Supplementary Files S2–S5. The Blender/Python implementation of HFPM and its common box-counting protocol is provided as S1; figure regeneration scripts are supplied as S6. The additional independent fixed-recursion, branch-pruning, density-seed, and grid-origin control data are included in S7, and the alternative scaling-window diagnostic data in S8. The described checks are numerical/geometric rather than independent structural or experimental validation.

Conflicts of Interest: The authors declare no conflicts of interest.

Abbreviations

The following abbreviations are used in this manuscript:

HFPM	Hybrid Fractal–Parametric Model
IFS	Iterated Function System
NSGA-II	Non-dominated Sorting Genetic Algorithm II
CAD	Computer-Aided Design
FEM	Finite Element Method
D_f	Finite-scale box-counting dimension estimate under the declared common protocol
A_s	Surface area
V_m	Modeled geometric material volume
R^2	Coefficient of determination

References

1. Shea, K.; Aish, R.; Gourtovaia, M. Towards integrated performance-driven generative design tools. *Autom. Constr.* **2005**, *14*, 253–264. [CrossRef]
2. Caldas, L.G.; Norford, L.K. A design optimization tool based on a genetic algorithm. *Autom. Constr.* **2002**, *11*, 173–184. [CrossRef]
3. Turrin, M.; von Buelow, P.; Stouffs, R. Design explorations of performance driven geometry in architectural design using parametric modeling and genetic algorithms. *Adv. Eng. Inform.* **2011**, *25*, 656–675. [CrossRef]
4. Mandelbrot, B.B. *The Fractal Geometry of Nature*; W.H. Freeman: San Francisco, CA, USA, 1982.
5. Barnsley, M.F. *Fractals Everywhere*, 2nd ed.; Academic Press: Boston, MA, USA, 1993. [CrossRef]
6. Hutchinson, J.E. Fractals and self similarity. *Ind. Univ. Math. J.* **1981**, *30*, 713–747. [CrossRef]
7. Falconer, K. *Fractal Geometry: Mathematical Foundations and Applications*, 2nd ed.; Wiley: Chichester, UK, 2003. [CrossRef]
8. Bovill, C. *Fractal Geometry in Architecture and Design*; Birkhäuser: Boston, MA, USA, 1996. [CrossRef]
9. Ostwald, M.J.; Vaughan, J. *The Fractal Dimension of Architecture*; Birkhäuser: Cham, Switzerland, 2016. [CrossRef]
10. Vaughan, J.; Ostwald, M.J. Fractal Geometry in Architecture. In *Handbook of the Mathematics of the Arts and Sciences*; Sriraman, B., Ed.; Springer: Cham, Switzerland, 2020; pp. 1–16. [CrossRef]
11. Ostwald, M.J. The fractal analysis of architecture: Calibrating the box-counting method using scaling coefficient and grid disposition variables. *Environ. Plan. B Plan. Des.* **2013**, *40*, 644–663. [CrossRef]

12. Foroutan-Pour, K.; Dutilleul, P.; Smith, D.L. Advances in the implementation of the box-counting method of fractal dimension estimation. *Appl. Math. Comput.* **1999**, *105*, 195–210. [CrossRef]
13. Katona, V. Relief method: The analysis of architectonic façades by fractal geometry. *Buildings* **2021**, *11*, 16. [CrossRef]
14. Katona, V. The hidden dimension of façades: Fractal analysis reveals composition rules in classical and Renaissance architecture. *Fractal Fract.* **2023**, *7*, 257. [CrossRef]
15. Lorenz, W.E.; Kulcke, M. Multilayered complexity analysis in architectural design: Two measurement methods evaluating self-similarity and complexity. *Fractal Fract.* **2021**, *5*, 244. [CrossRef]
16. Kulcke, M.; Lorenz, W.E. Spherical box-counting: Combining 360° panoramas with fractal analysis. *Fractal Fract.* **2023**, *7*, 327. [CrossRef]
17. Ma, L.; He, S.; Lu, M. A measurement of visual complexity for heterogeneity in the built environment based on fractal dimension and its application in two gardens. *Fractal Fract.* **2021**, *5*, 278. [CrossRef]
18. Tara, A.; Patuano, A.; Lawson, G. Between 2D and 3D: Studying structural complexity of urban fabric using voxels and LiDAR-derived DSMs. *Fractal Fract.* **2021**, *5*, 227. [CrossRef]
19. Ali, L.A.; Mustafa, F.A. Fractal dimensional analysis of building facades: The case of office buildings in Erbil City. *Fractal Fract.* **2024**, *8*, 746. [CrossRef]
20. Zhang, C.; Ping, X.; Fan, Q.; Li, C. Measurement of 2D and 3D fractal features of urban morphology from an architectural view and its influencing factors. *Fractal Fract.* **2024**, *8*, 138. [CrossRef]
21. Wang, J.; Yang, G.; Yuan, Y.; Sun, J.; Pu, G. Effects of Scale Parameters and Counting Origins on Box-Counting Fractal Dimension and Engineering Application in Concrete Beam Crack Analysis. *Fractal Fract.* **2025**, *9*, 549. [CrossRef]
22. Douglass, R.W. Automated Box-Counting Fractal Dimension Analysis: Sliding Window Optimization and Multi-Fractal Validation. *Fractal Fract.* **2025**, *9*, 633. [CrossRef]
23. Wang, W.; Zmeureanu, R.; Rivard, H. Applying multi-objective genetic algorithms in green building design optimization. *Build. Environ.* **2005**, *40*, 1512–1525. [CrossRef]
24. Wang, L.; Wong, N.H.; Li, S. Facade design optimization for naturally ventilated residential buildings in Singapore. *Energy Build.* **2007**, *39*, 954–961. [CrossRef]
25. Magnier, L.; Haghighat, F. Multiobjective optimization of building design using TRNSYS simulations, genetic algorithm, and Artificial Neural Network. *Build. Environ.* **2010**, *45*, 739–746. [CrossRef]
26. Evins, R. A review of computational optimisation methods applied to sustainable building design. *Renew. Sustain. Energy Rev.* **2013**, *22*, 230–245. [CrossRef]
27. Nguyen, A.-T.; Reiter, S.; Rigo, P. A review on simulation-based optimization methods applied to building performance analysis. *Appl. Energy* **2014**, *113*, 1043–1058. [CrossRef]
28. Machairas, V.; Tsangrassoulis, A.; Axarli, K. Algorithms for optimization of building design: A review. *Renew. Sustain. Energy Rev.* **2014**, *31*, 101–112. [CrossRef]
29. Yi, Y.K. Building facade multi-objective optimization for daylight and aesthetical perception. *Build. Environ.* **2019**, *156*, 178–190. [CrossRef]
30. Bianchi, S.; Andriotis, C.; Klein, T.; Overend, M. Multi-criteria design methods in façade engineering: State-of-the-art and future trends. *Build. Environ.* **2024**, *250*, 111184. [CrossRef]
31. Zhang, J.; Liu, N.; Wang, S. Generative design and performance optimization of residential buildings based on parametric algorithm. *Energy Build.* **2021**, *244*, 111033. [CrossRef]
32. Wang, B.; Lu, W.; Zhang, Y. A graph-enabled parametric modeling approach for façade layout generative design. *J. Build. Eng.* **2025**, *105*, 112481. [CrossRef]
33. Wefki, H.; Salah, M.; Elbeltagi, E.; Alinizzi, M. Generative design-driven optimization for effective concrete structural systems. *Buildings* **2025**, *15*, 2646. [CrossRef]
34. Prusinkiewicz, P.; Lindenmayer, A. *The Algorithmic Beauty of Plants*; Springer: New York, NY, USA, 1990. [CrossRef]
35. Rvachev, V.L. *Teoriya R-Funktsiy i Nekotoryye Yeye Prilozheniya [The R-Functions Theory and Some of Its Applications]*; Naukova Dumka: Kyiv, Ukraine, 1982.
36. Anarova, S.; Narzulloev, O.; Ibragimova, Z. Development of fractal equations of national design patterns based on the method of R-function. *Int. J. Innov. Technol. Explor. Eng.* **2020**, *9*, 134–141. [CrossRef]
37. Anarova, S.A.; Ibrohimova, Z.E. Methods of constructing equations for objects of fractal geometry and R-function method. In *Intelligent Human Computer Interaction*; Lecture Notes in Computer Science; Springer: Cham, Switzerland, 2022; Volume 13184, pp. 425–436. [CrossRef]
38. Anarova, S.; Azimbayevna, S.S.; Berdiev, G.; Ilhomjon Ogli, A.T.; Ilxom Kizi, M.I. Geometric modelling of fractal structured objects based on integration of R-function and L-system methods. In *Proceedings of the ACM International Conference Proceeding Series*; Association for Computing Machinery: New York, NY, USA, 2024; pp. 172–181. [CrossRef]

39. Rian, I.M.; Asayama, S. Computational design of a nature-inspired architectural structure using the concepts of self-similar and random fractals. *Autom. Constr.* **2016**, *66*, 43–58. [CrossRef]
40. Rian, I.M.; Sassone, M.; Asayama, S. From fractal geometry to architecture: Designing a grid-shell-like structure using the Takagi–Landsberg surface. *Comput.-Aided Des.* **2018**, *98*, 40–53. [CrossRef]
41. Rian, I.M.; Sassone, M. Tree-inspired dendriforms and fractal-like branching structures in architecture: A brief historical overview. *Front. Archit. Res.* **2014**, *3*, 298–323. [CrossRef]
42. Rian, I.M.; Sassone, M. Fractal-based generative design of structural trusses using iterated function system. *Int. J. Space Struct.* **2014**, *29*, 181–191. [CrossRef]
43. Anarova, S.; Sadullaeva, S.A.; Berdiev, G. Calculation of building dimensions in the method of composition fractal analysis. In Proceedings of the 2021 International Conference on Information Science and Communications Technologies (ICISCT), Tashkent, Uzbekistan, 3–5 November 2021. [CrossRef]
44. Wang, H.; Guo, T.; Zhang, Z. Generative design and evaluation of spatial grid structures based on parametric topology optimization driven by metaheuristic algorithms. *Eng. Struct.* **2026**, *358*, 122655. [CrossRef]
45. Nouri, L.; Taghizadeh Azari, K.; Pourfouladi, M.; Keramat, D.; Alaghmandan, M. Form-finding and optimization of branching columns using L-systems in early stages of design: A parametric approach. *J. Build. Eng.* **2026**, *117*, 114817. [CrossRef]
46. Deb, K.; Pratap, A.; Agarwal, S.; Meyarivan, T. A fast and elitist multiobjective genetic algorithm: NSGA-II. *IEEE Trans. Evol. Comput.* **2002**, *6*, 182–197. [CrossRef]
47. Zitzler, E.; Deb, K.; Thiele, L. Comparison of multiobjective evolutionary algorithms: Empirical results. *Evol. Comput.* **2000**, *8*, 173–195. [CrossRef] [PubMed]
48. Coello Coello, C.A. Evolutionary multi-objective optimization: A historical view of the field. *IEEE Comput. Intell. Mag.* **2006**, *1*, 28–36. [CrossRef]
49. Blank, J.; Deb, K. pymoo: Multi-objective optimization in Python. *IEEE Access* **2020**, *8*, 89497–89509. [CrossRef]
50. McKay, M.D.; Beckman, R.J.; Conover, W.J. A Comparison of Three Methods for Selecting Values of Input Variables in the Analysis of Output from a Computer Code. *Technometrics* **1979**, *21*, 239–245. [CrossRef]
51. Eshelman, L.J.; Schaffer, J.D. Real-Coded Genetic Algorithms and Interval-Schemata. In *Foundations of Genetic Algorithms 2*; Whitley, L.D., Ed.; Morgan Kaufmann: San Mateo, CA, USA, 1993; pp. 187–202. [CrossRef]

Disclaimer/Publisher's Note: The statements, opinions and data contained in all publications are solely those of the individual author(s) and contributor(s) and not of MDPI and/or the editor(s). MDPI and/or the editor(s) disclaim responsibility for any injury to people or property resulting from any ideas, methods, instructions or products referred to in the content.